Transient Electron Spin Polarization Imaging of Heterogeneous Charge-Separation Geometries at Bulk-Heterojunction Interfaces in Organic Solar Cells

Kobori, Yasuhiro
Ako, Takumi
Oyama, Shinya
Tachikawa, Takashi
Marumoto, Kazuhiro

(Citation)
Journal of Physical Chemistry C,123(22):13472-13481

(Issue Date)
2019-07-06

(Resource Type)
journal article

(Version)
Version of Record

(URL)
https://hdl.handle.net/20.500.14094/90006237

THE JOURNAL OF PHYSICAL CHEMISTRY C

Article

Cite This: J. Phys. Chem. C 2019, 123, 13472−13481

pubs.acs.org/JPCC

Transient Electron Spin Polarization Imaging of Heterogeneous Charge-Separation Geometries at Bulk-Heterojunction Interfaces in Organic Solar Cells

Yasuhiro Kobori,*[,†,‡] Takumi Ako,[‡] Shinya Oyama,[‡] Takashi Tachikawa,[†,‡] and Kazuhiro Marumoto[§,∥]

[†]Molecular Photoscience Research Center and [‡]Department of Chemistry, Graduate School of Science, Kobe University, 1-1 Rokkodai-cho, Nada-ku, Kobe 657-8501, Japan

[§]Division of Materials Science, University of Tsukuba, Tsukuba, Ibaraki 305-8573, Japan

[∥]Tsukuba Research Center for Energy Materials Science (TREMS), University of Tsukuba, Tsukuba, Ibaraki 305-8571, Japan

Supporting Information

ABSTRACT: Despite the importance of elucidating photoinduced charge-generation mechanisms for the development of efficient organic solar cells (OSC), it has been quite difficult to characterize molecular geometries, electronic couplings, and charge mobilities in the initial photoinduced charge-separated (CS) states for the heterogeneous molecular environments in bulk-heterojunction interfaces between electron donor−acceptor domains in the photoactive layers. In this study, we employed a time-resolved electron paramagnetic resonance method to characterize two kinds of electron spin polarizations (ESPs) of the photoinduced CS states as different geometries, exchange couplings, and spin-relaxation times of spin-correlated radical pairs in OSC blend films composed of regioregular poly(3-hexylthiophene-2,5-diyl) and [6,6]-phenyl-C_{61}-butyric acid methyl ester by applying polarized light excitations (magnetophotoselection) with respect to an external magnetic field direction at a cryogenic temperature. From this, we performed analysis of mapping the ESPs to space directions to obtain image views of the molecular geometries in mobile and trapped CS states. We propose that the heterogeneities in the interfacial charge generations may be correlated with high- and low-frequency phonon modes leading to the mobile and weakly trapped charge pairs, respectively, denoting the great significance of such molecular motions for the efficient photocarriers overcoming the interfacial electrostatic binding potential.

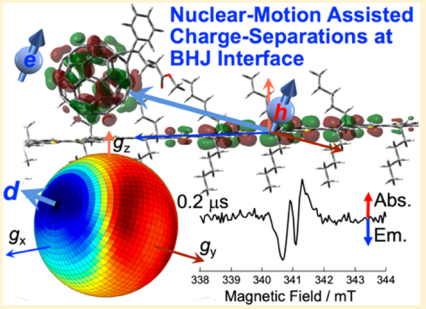

INTRODUCTION

The organic solar cells (OSC) have attracted great attention because of low cost, nontoxicity, and flexibility compared to the other types of solar cells. Recent remarkable progress in organic materials related to the organic semiconductors has achieved a power conversion efficiency (PCE) close to 15%[1,2] for single junction cells, although the PCE is still lower than the recent developments of 22−23% in the solar cells employing organolead halide perovskites.[3]

Solid-state photoactive layers have been fabricated by spin-coating of mixed solutions composed of the conjugated polymer as an electron donor (D) and an organic acceptor (A) material for generating the photocarrier in OSC. The photoactive layer of the blend film usually forms the bulk-heterojunction (BHJ) D:A interfaces by the phase segregation of self-organized domains.[4] This BHJ plays a key role in the initial photoinduced charge separation (CS) following exciton migrations to the domain interfaces. Despite recent progress in molecular designs tuning organic optoelectronic and structural properties for the higher PCEs,[1,5−7] the mechanism of the initial photocarrier generation is poorly understood even in the well-studied poly(alkylthiophene):PCBM systems (Scheme 1).

Scheme 1. Structure Formula of P3HT and $PC_{61}BM$ Utilized for OSC

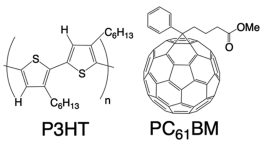

Several studies discussed why and how the electron and hole escape from the charge transfer (CT) binding interaction at the domain interface.[8−15] It was pointed, as an example, that such a binding energy is overcome by entropy enhancement due to an increase in the possible sites of the separated charges after the CT state.[11,14] The importance of the electron−phonon (e−p) interactions was also discussed to promote the dissociations by molecular motions.[16−21] The orbital delocalization is another origin of the charge conductions.[13,15,18,22,23]

Received: March 21, 2019
Revised: May 11, 2019
Published: May 15, 2019

DOI: 10.1021/acs.jpcc.9b02672
J. Phys. Chem. C 2019, 123, 13472−13481

Hodgkiss and co-workers[24] demonstrated distance distributions in photogenerated charge pairs using transient absorption spectroscopy at cryogenic temperature for blend films. It was shown that ca. 1 and 3−4 nm separated pairs were both generated at the interface, demonstrating the highly disordered interfacial molecular environment for the photocarrier generation in the blend materials. Kassal and co-workers[11] theoretically predicted that energetic disorder may enable the exergonic CS while delocalization by chromophore coupling would induce a barrier height for the CS.[13] However, the geometrical and energetic disorders are not experimentally characterized on the transient CS states.

The time-resolved electron paramagnetic resonance (TREPR) method is powerful for characterizing distances and geometries in photoinduced charge pairs, as recently demonstrated for the primary CS state[25] in plant photosystem II. As shown in Figure 1, electron spin polarization (ESP)

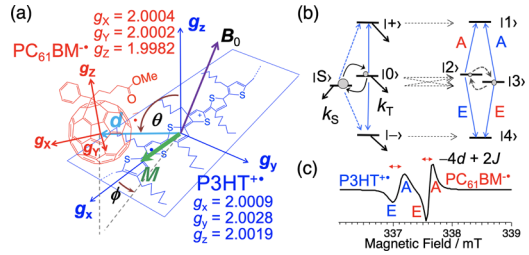

Figure 1. (a) Setting of the geometries in the interfacial CS state reflecting anisotropies of the *g*-tensors[35−37] and the spin−spin dipolar coupling in the present study. Principal axes and their values are depicted for the *g*-tensors. The principal axis of the dipolar interaction is represented by ***d*** as the inter-spin vector. The anisotropies in the hyperfine interactions of $P3HT^{+\bullet}$ were also considered.[18,21] ***M*** denotes the direction of the transition dipole moment[38] memorized by the one-dimensional (1D) exciton diffusion after polarized laser excitation ***L***. (b) Schematic SCRP model based on the singlet (S) and the triplet (+, 0, and −) sublevels of the radical pair. S−T_0 mixing by the hyperfine interaction and by the Δg ($=g_{P3HT} - g_{PCBM}$) causes four EPR transitions (denoted by A and E) in the right because the S−$T_{\pm}$ forbidden transitions (dashed allows in the left) are mixed with the allowed T_0−$T_{\pm}$ transitions.[39,40] (c) The EPR transition peaks by the two antiphase doublets at one specified $\boldsymbol{B}_0$ direction from the SCRP model. The peak splittings[29] denoted by the arrows reflect $-4d + 2J$, where d [$=D(\cos^2\theta_D - 1/3)/2$] and J ($=62\ \mu$T) are the dipolar and exchange interactions, respectively, with $D < 0$. k_S and k_T are the recombination rates to the ground state and to the excited triplet state (^{3}P3HT*), respectively.

detected as microwave absorption (A) and emission (E) from spin-states of spin-correlated radical pairs (SCRP)[26−29] is often sensitive to directions ($\boldsymbol{B}_0$) of external magnetic field in a molecular-pair coordinate system because of the several spin anisotropic characters in the transient $D^{+\bullet}\cdots A^{-\bullet}$ states. Therefore, one may obtain the geometrical parameters in the transient charge pairs (Figure 1a) by analyzing the SCRP spin polarizations (Figure 1b,c). Recently, the electron spin polarization imaging (ESPI) method to map the ESP for several $\boldsymbol{B}_0$-directions has been presented for clear visualization of geometries of the transient CS state in a direct way.[25] From TREPR spectrum analysis of the SCRP polarization obtained in a frozen solution and in oriented multilayers of thylakoid membranes, the anisotropy of the spin−spin dipolar coupling was mapped to a three-dimensional $\boldsymbol{B}_0$-direction space to characterize the positions and orientation of the primary CS state in the membrane.

In our previous studies,[16,18,21] geometries and electronic couplings of the CS states were estimated at the BHJ interfaces by analyses of the SCRP polarization (Figure 1b) for D:A blend thin films composed of regioregular poly(3-hexylthiophene-2,5-diyl) (P3HT) and [6,6]-phenyl-C_{61}-butyric acid methyl ester ($PC_{61}BM$) in Scheme 1. The disordered D/A interfacial molecular environment in the conformations and in the energies might, however, challenge the validities of the determinations of the magnetic parameters related to the CS geometries and their interactions,[30] even though these properties were regarded as ensemble averaged characteristics. Moreover, the ESP patterns (the E/A/E/A or A/E/A/E in the EPR transitions from the lower B_0 field) in Figure 1c varied with reports presented by several groups[18,21,30−34] even though the blend materials and their D:A blend ratios are fairly common. This would reflect the difference in the morphology of the fabricated film to influence the dominant ESP spectrum pattern because the ESP is sensitive to the CS geometry and to the exchange interaction (J) between the two spins as shown in Figure 1c.[30] Alternatively, EPR cavity conditions influenced by temperature, measurement materials, and intrinsic microwave power (B_1 field) would alter the susceptibility of the ESP detections of those complex species depending on the heterogeneity in the phase memory times (T_2) in these spin systems. Despite the importance of understanding the initial charge conduction mechanism, the heterogeneities in charge positions, orientations, and electronic couplings are not established together with the motions in the initial CS states. One may thus raise the following questions. (1) Can the heterogeneous geometries, motions, and electronic characters be experimentally distinguished for the interfacial CSs? (2) How are these characteristics related to the charge conduction in OSC?

It is also very important to obtain the geometries and the electronic coupling in the transient CS state not only in the blend films but also in the cell device. Marumoto and co-workers reported pioneering works on characterizing long-lived trapped carriers using the steady-state EPR method at the interfaces between the photoactive layers and the hole transport layers of PEDOT:PSS.[41] In this, the trapped charges were reported to be accumulated by continuous light irradiation in the device structures or device substrates, lowering the device performance. On the other hand, the geometries and electronic properties of the short-lived transient CS states have not yet been characterized in the OSC substrate.

In the present study, we have measured and analyzed the TREPR spectra from a substrate of a cell device composed of indium tin oxide (ITO)/PEDOT:PSS/P3HT:$PC_{61}BM$/LiF/Al, where ITO and Al are cathode and aluminum anode, respectively. We characterized the interfacial CS geometries and their electronic couplings in the active layer by supporting detections of light polarization direction (***L***) effect of the excitation laser on the TREPR spectrum with respect to the B_0 direction on the P3HT:$PC_{61}BM$ blend films applying $\boldsymbol{L} \parallel \boldsymbol{B}_0$ and $\boldsymbol{L} \perp \boldsymbol{B}_0$. This ***L*** effect has been referred to as magnetophotoselection (MPS) and has long been demonstrated to be useful to determine the orientations of the spin−spin dipolar interactions.[42−46] We herein characterized two different TREPR components possessing different spin−spin

DOI: 10.1021/acs.jpcc.9b02672
J. Phys. Chem. C 2019, 123, 13472−13481

geometries and relaxation times in the CS states due to the disorders.

METHODS

Chemicals and Sample Preparations. P3HT (Sigma-Aldrich), $PC_{61}BM$ (>99.5%, Tokyo Kasei), and 1,2-dichlorobenzene (>99%, Tokyo Kasei) were used as received without further purification. On the MPS measurements, the BHJ thin films were fabricated by the spin-coating of the solutions on thin cover glasses with 1 cm^2 using a spin coater (Mikasa MS-A100). The films were then manually treated within a powder paper to produce a number of broken tips of ca. 0.5 mm^2 and were placed in the EPR sample tubes (Figure S1). The films were then deaerated using a vacuum line under the vacuum pressures of 10^{-3} Pa to remove solvent and oxygen in the films. After evaporation, the 1:1 glycerol/water (v/v) mixture was added to the EPR tube to ensure the film temperature and to protect the films from the ablation damage by laser irradiation. The freeze−pump−thaw cycles were performed to deoxygenate the solutions using the vacuum line. The device fabrication was performed as reported previously.[41] No annealing procedures were performed before the TREPR measurements. The OSC device was sealed under dry a nitrogen atmosphere in an EPR sample tube before the TREPR measurements.

Time-Resolved EPR Measurements. The X-band TREPR measurements were carried out using a Bruker EMX Plus system without using the field modulations. In the microwave bridge, a modified wide-band preamplifier was equipped. Light excitations were performed by the second harmonics (532 nm) of an Nd:YAG laser (Continuum, Minilite II, fwhm ∼5 ns). A laser depolarizer (SIGMA KOKI, DEQ 1N) was placed between the laser exit and the microwave cavity for the depolarized TREPR data. Transient EPR signals were averaged by a Tektronix DPO3054 500 MHz digital phosphor oscilloscope at 201 different external magnetic field positions and were transferred to a personal computer via a USB communication to obtain the two-dimensional TREPR data. The sample tubes were placed in a liquid nitrogen Dewar flask filled with the liquid nitrogen and was fixed inside the EPR cavity for the MPS measurements for the spin-coated film. For the substrate of the OSC, temperature (98 K) was controlled using a nitrogen gas-flow system.

Numerical Simulations. Numerical calculations and the ESPI[25] mappings were performed using MATLAB (The MathWorks). The computation methods to obtain the delay time (t_d) dependence of the TREPR spectra[21,25,39] and the time profiles[18] of the transverse magnetizations were reported previously for the transient CS states. We also set a precursor CS state[30] in which density matrix elements of coherence terms (ρ_{0S} and ρ_{S0}) in an S−T_0 system developed within a nanosecond lifetime in the presence of a strong exchange coupling (J_{pre} = 0.4 mT). Then, such coherence terms together with the populations (ρ_{SS} and ρ_{00}) were transferred to the corresponding density matrix elements of the two different SCRPs, as shown in Figure 1b, to generate the density matrix elements of the initial conditions.[47] This will produce an overlapping net "E" polarization at the $P3HT^{+\bullet}$ resonance side and a net "A" at the higher field $PC_{61}BM^{-\bullet}$ side in Figure 1c, which is referred to as the chemically induced dynamic electron polarization (CIDEP) from the precursor radical pairs.[47−49] This CIDEP effect has, however, been revealed to be minor with respect to the SCRP contributions (Figure 1c) under the X-band TREPR measurements. For MPS analysis,[42] the ESP signals (ESP^0_{para} and ESP^0_{perp}) for $\boldsymbol{B}_0$ // $\boldsymbol{L}$ and $\boldsymbol{B}_0$ ⊥$\boldsymbol{L}$ were set to be proportional to the squares of direction cosines and to the halves of the squares of the sine components, respectively, between the $\boldsymbol{B}_0$ and $\boldsymbol{M}$ vectors as shown in Figure 1. A depolarization effect[46] (ξ = 0.38 in $0 \le \xi \le 1$) was introduced to compute $ESP_{para} = (1-\xi)ESP^0_{para} + \xi(ESP^0_{para} + 2ESP^0_{perp})$ and $ESP_{perp} = (1-\xi)ESP^0_{perp} + \xi(ESP^0_{para} + 2ESP^0_{perp})$ for fitting the $\boldsymbol{B}_0$ // $\boldsymbol{L}$ and $\boldsymbol{B}_0$ ⊥ $\boldsymbol{L}$ spectra, respectively. A value of ξ = 0.35 was obtained to reproduce the MPS effect for another as-spun film (Figure S4). The ξ effect originates from depolarization of $\boldsymbol{M}$ by partially disordered exciton migrations, as detailed below.

The orientations of the g-tensors in $PC_{61}BM^{-\bullet}$ (Figure 1) were set by the Euler angles (Table S1) with respect to the principal axis system in $P3HT^{+\bullet}$, as reported previously.[18] In principle, one could find the angle parameter sets to eliminate the laser polarization effects on the higher-field antiphase doublets created by the $PC_{61}BM^{-\bullet}$ conformation. Thus, these Euler parameters might be treated as artifacts created during the spectrum fitting procedures because acceptor conformations are supposed to be highly disordered at the interface,[50] as described below.

RESULTS AND DISCUSSION

Samples and Crystallinity. We prepared the OSC with the substrate of ITO (150 nm thickness)/PEDOT:PSS (ca. 40 nm)/P3HT:$PC_{61}BM$ (ca. 160 nm)/LiF (0.6 nm)/Al (100 nm), as reported previously.[41] For the photoactive layer, ca. 3 wt % of P3HT:$PC_{61}BM$ = 1.0:0.8 (w/w) mixture solution in 1,2-dichlorobenzene was spin-coated on the PEDOT:PSS layer at 1000 rpm for 75 s to form ca. 160 nm thick films. We alternately prepared the P3HT:$PC_{61}BM$ film with the ca. 160 nm thickness using 1.0:0.7 (w/w) mixture solution in 1,2-dichlorobenzene fabricated by the spin-coating on cover glasses with 1000 rpm for 50 s. The present smaller spinning rates and the higher P3HT contents ensure higher crystallinity of the P3HT domain than in the spin-coated films of the previous TREPR report[21] on the 1:1 (w/w) blend films fabricated by the 3000 rpm rates. More details on the materials are described in the Method section and in Figure S1. Figure 2 shows the ground-state absorption spectrum of the as-spun blend films. The strong absorption bands at the 500−600 nm region correspond to the transitions of the self-organized crystalline phase of P3HT, as reported previously,[51] indicating the predominant crystallinity of the P3HT domain in the

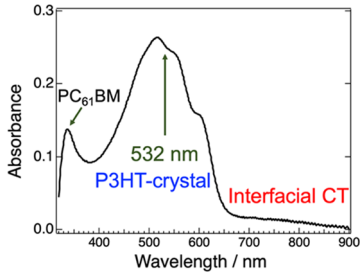

Figure 2. Ground-state absorption spectrum of the as-spun P3HT:$PC_{61}BM$ (1.0:0.7 weight ratio) blend film used for the MPS measurements. The 532 nm laser was employed to selectively pump the P3HT-crystalline domain. The interfacial CT band is also observed around 800 nm.

DOI: 10.1021/acs.jpcc.9b02672
J. Phys. Chem. C 2019, 123, 13472−13481

present study. To obtain the MPS effects, the light excitations were performed by the second harmonics (532 nm) of an Nd:YAG laser to dominantly photoexcite the crystalline phase of the P3HT domain of the blend film (Figure 2).

TREPR Data of the OSC Substrate. Figure 3 shows the TREPR data obtained by the 532 nm laser excitation of the ITO/PEDOT:PSS/P3HT:$PC_{61}BM$/LiF/Al substrate of the OSC at T = 98 K. In this experiment, depolarized light pulses were employed. It is evident that the TREPR spectrum is dramatically changed by the delay time (t_d) after the laser flash in Figure 3a–c and is similar to the previous TREPR study on 1:1 P3HT:$PC_{61}BM$ composites reported by Behrends and co-workers.[32] The TREPR spectrum exhibits an E/A/E/A pattern that was assigned to the transient interfacial CS state. On the other hand, an inverted A/E/A/E-polarized EPR spectrum emerges at t_d = 0.6 μs, as was predominantly observed in the previous study for the films spun at 3000 rpm.[21] These E/A/E/A and A/E/A/E-polarized EPR spectra were both interpreted by the SCRP model contributed by the spin–spin dipolar coupling (d) and by J as shown in Figure 1c.[18,32,33]

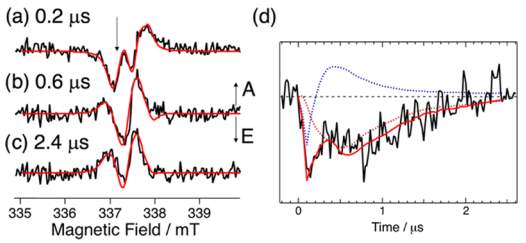

Figure 3. (a–c) Delay time dependence of the TREPR spectrum by 532 nm laser irradiation of the substrate from ITO/PEDOT:PSS/P3HT:$PC_{61}BM$/LiF/Al of the OSC obtained at 98 K, showing E/A/E/A (0.2 μs) and A/E/A/E (>0.6 μs) patterns. (d) Time profile of the TREPR signal at 337.2 mT as indicated by the arrow in (a). These data were obtained at open-circuit conditions. Solid red lines were obtained by stochastic-Liouville equation (SLE) analysis of the SCRP model using the two different CS state components as shown by the decomposed dotted profiles in (d).

This suggests that the two SCRP components possessing different combinations of D and J parameters are generated. Here, D represents the dipolar coupling constant in $d = D(\cos^2\theta_D - 1/3)/2$ that determines the peak splitting depending on θ_D, i.e., the angle between $\boldsymbol{B}_0$ and $\boldsymbol{d}$ in Figure 1a. The A/E/A/E spectrum was explained by a strong D (≈−500 μT) with respect to J (≈10 μT).[21] Figure 3d shows the time profile of the TREPR intensity at the field position (337.2 mT) indicated by the arrow in Figure 3a. The emissive EPR signal initially rises within 0.1 μs but decays with ≈0.2 μs time constant. This quick component corresponds to the E/A/E/A spectrum as shown in Figure 3a. Subsequently, the slower rise in the component in the E signal is observed around 0.5 μs and decays at 2 μs, corresponding to the A/E/A/E spectrum as shown in Figure 3b. After the decay of this emissive polarization, an absorptive EPR spectrum was observed at t_d = 2.4 μs in Figure 3c, denoting that the spin–lattice relaxation time of T_1 (=1.1 μs) is responsible for the decay of the E polarization resulting in the absorptive thermal equilibrium sublevel population in Figure 1b. Thus, the quick decay in the E/A/E/A component denotes that T_1 (=0.3 μs) is small indicating that a mobile electron–hole pair is generated. In contrast, the A/E/A/E component with T_1 = 1.1 μs in Figure 3b is attributable to a shallowly trapped charge pair with the separation distance of r_{CC} ≈ 1.7 nm, as we concluded previously for the A/E/A/E polarization.[16,21]

Magnetophotoselection of the TREPR Spectrum of Blend Films. For understanding the geometrical properties for the above two transient CS states, we observed the MPS effects for the blend film, as shown in Figure 4. The E/A/E/A polarizations were detected only at the early stage of t_d = 0.2 μs in Figure 4, which were very similar to the result in Figure 3. The E/A/E/A effect was most prominent when $\boldsymbol{L}$ is perpendicular to the $\boldsymbol{B}_0$ direction (Figure 4b), while the inner A/E contribution around the center field became weak when $\boldsymbol{L}$ is parallel to $\boldsymbol{B}_0$ (Figure 4c). Additionally, the emission peak position at the lower field indicated by the arrow in Figure 4b is situated to be lowest, while the corresponding peak is highest in Figure 4c among the spectra in Figure 4a–c.

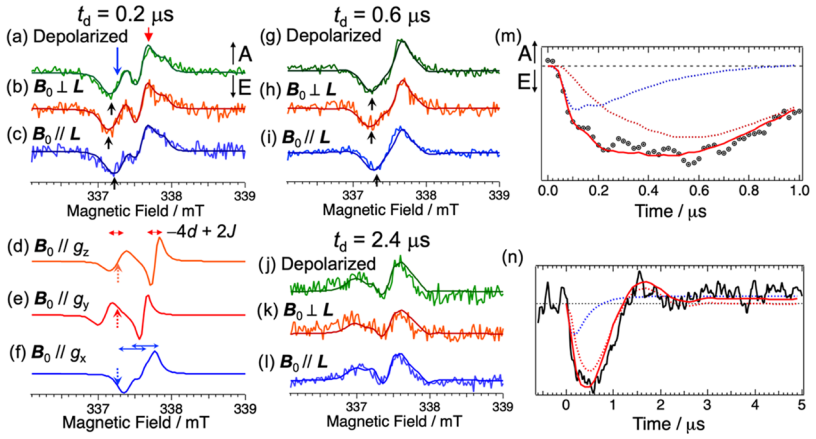

Figure 4. (a–c) Magnetophotoselection effects of the TREPR spectrum for the delay time of t_d = 0.2 μs by 532 nm laser irradiation of the blend film of P3HT:$PC_{61}BM$ at 77 K. The microwave power was 6.3 mW. (d–f) Computed EPR spectra of the SCRP for the field directions to the principal axes (g_x, g_y, g_z) in $P3HT^{+\bullet}$ by applying J = 62 μT, D = −100 μT, θ = 65°, and ϕ = 0° in Figure 1a. (g–l) MPS effects for the later delay times of t_d = 0.6 and 2.4 μs. (m, n) Time profiles of the TREPR signal at B_0 = 337.30 mT for the depolarized conditions. Computed profiles are shown by the red solid lines obtained by SLE analysis. The red lines were decomposed to the mobile CS state (dotted blue lines computed with T_1 = 0.4 μs and T_2 < 0.2 μs) and to the trapped CS state (dotted red lines, T_1 = 1.6 μs and T_2 = 3.0 μs), respectively. Respective spectrum components are shown in Figure S2.

DOI: 10.1021/acs.jpcc.9b02672
J. Phys. Chem. C 2019, 123, 13472–13481

Because these resonance positions at the lower field reflect a P3HT$^{+\bullet}$ resonance side in the SCRP due to $g_{P3HT} > g_{PCPM}$, as shown by the blue E/A transitions in Figure 1b,c, the MPS effect on the peak position is ascribed to the anisotropy in g_{P3HT}. This implies that the P3HT$^{+\bullet}$ conformations in the interfacial CS states memorize the $\boldsymbol{L}$ polarizations excited in the P3HT domains, i.e., one-dimensional singlet exciton diffusions to the domain interface (Figure 5b) and the

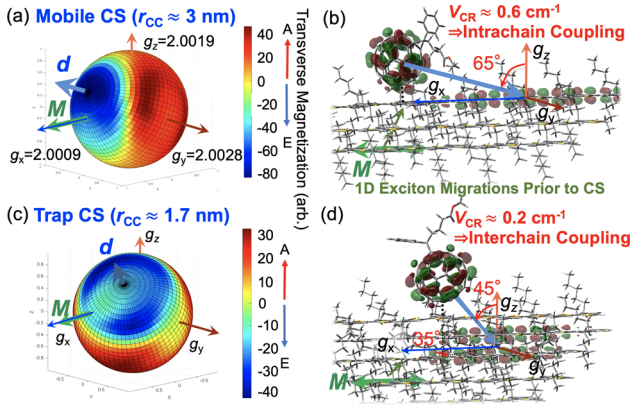

Figure 5. Interfacial photoinduced charge-separation geometries (b, d) characterized by ESPIs (a, c) from the E/A/E/A pattern at 0.2 μs and from A/E/A/E at 0.6 μs, respectively. The ESPIs in (a) and (c) were obtained by distributing the transverse magnetization (ESP intensities in Figure 4d–f) at B_0 = 337.25 mT as the color maps to the $\boldsymbol{B}_0$ space directions in the electron–hole pairs generated after the migrations of the exciton ($\boldsymbol{M}$) to the P3HT-crystal/PCBM interfaces. The hole geometries in (b) and (d) are schematically drawn based on a tilted packing structure with short π–π stackings of 0.34 nm interplanar distances in the crystalline P3HT obtained by the electron diffraction analysis.[55] Inter-spin distances (r_{CC}) and electronic couplings (V_{CR}) were estimated from D and J, respectively.

subsequent interfacial CS cause the shifts in the peak positions in Figure 4a–c. The one-dimensional exciton ($\boldsymbol{M}$ in Figure 1a) migration was demonstrated by Ohkita and co-worker[51] in the spin-coated P3HT films possessing the crystallinity that is presently consistent with the intense absorption band around 600 nm by the crystalline phase as shown in Figure 2. Furthermore, P3HT-crystal/PCBM interfacial domains were clarified by grazing-incidence small-angle and wide-angle X-ray scattering measurements in the blend films.[50] These coincide with the above MPS results because the 1D exciton migration to the interface may result in the preferential generations of the ordered P3HT$^{+\bullet}$ memorized by $\boldsymbol{L}$ in the interfacial CS states.

Because the optical transition dipole moment ($\boldsymbol{M}$) is parallel to the long axis (g_x direction in P3HT$^{+\bullet}$)[37,38] of the polymer as shown in Figure 1a, the orientations of the g tensor and of the $\boldsymbol{d}$ interaction are estimated from the SCRP model, as follows. The higher field position of the emission peak in the $\boldsymbol{B}_0$ // $\boldsymbol{L}$ situation (Figure 4c) denotes that the g_x direction (g_x = 2.0009) is parallel to $\boldsymbol{M}$, while the g_y = 2.0028 and g_z = 2.0019 directions are perpendicular to the $\boldsymbol{M}$ vector, as in Figure 1a because $\boldsymbol{M}$ tends to be aligned with the $\boldsymbol{L}$ direction. When the inter-spin $\boldsymbol{d}$ vector is close to the g_x direction and $\boldsymbol{B}_0$ is aligned to g_x, the peak splitting determined by $-4d + 2J$ in Figure 1c is greater than the splitting for the other $\boldsymbol{B}_0$ alignments because $-4d \approx -4D/3$ (>0) is large and may exceed $2J$ (>0) due to $\theta_D \approx 0$ in $d = D(\cos^2\theta_D - 1/3)/2$. This larger E/A splitting in each antiphase doublet causes intensity cancellation in the inner A/E transitions of the E/A/E/A pattern, as calculated by the SCRP model in Figure 4f with J = 62 μT, D = −100 μT, θ = 65°, and ϕ = 0°. On the other hand, in the $\boldsymbol{B}_0 \perp \boldsymbol{L}$ situation, the $\boldsymbol{d}$ vector tends to be close to the magic angle of θ_D = 54.7° with respect to $\boldsymbol{B}_0$ lying mainly in the g_y and g_z directions in Figure 1a. In this case, the peak splitting is dominated by $2J$ resulting in the sharp E/A/E/A pattern, as computed in Figure 4d,e. It is noted that the sum of the spectra in Figure 4d,e is close to the spectrum of Figure 4b and that the spectrum Figure 4c is also very similar to the spectrum computed for the g_x direction (Figure 4f). This denotes that the MPS effect is well explained by the $\boldsymbol{d}$ vector residing close to the g_x axis, as in a situation in Figure 1a. From this geometry, the distant CS state is concluded to be generated via the intrachain hole conduction after the contact CT[52] at the domain interface. As for the higher field E/A component attributed to the PC$_{61}$BM$^{-\bullet}$ resonance (Figure 1c) in Figure 4a–c, the peak position indicated by the red arrow in Figure 4a is unchanged by $\boldsymbol{L}$, suggesting that the PC$_{61}$BM$^{-\bullet}$ conformations (red axes system in Figure 1a) are disordered with respect to the P3HT$^{+\bullet}$ coordinate system (blue axes in Figure 1a) residing at the crystalline domain. This probably reflects heterogeneous PC$_{61}$BM interfacial conformations at the BHJ as opposed to the ordered polymer crystalline feature.

At the larger delay time (t_d = 0.6 μs in Figure 4g–i), no apparent MPS effect is observed on the A/E/A/E polarization overlapping to the E/A/E/A, as described below. However, the emissive peak position in the P3HT$^{+\bullet}$ resonance side is still dependent on the $\boldsymbol{L}$ direction, suggesting that the P3HT$^{+\bullet}$ part in the CS state has the memory of $\boldsymbol{L}$ polarization, as indicated by the arrows in Figure 4g–i. A similar trend was obtained for the lower-field peaks at t_d = 2.4 μs, although the absorptive signals by the thermal equilibrium spin population became dominant overlapping the A/E/A/E spin polarization in Figure 4j–l. Figure 4m,n display the time profiles of the TREPR signal at 337.25 mT indicated by the blue arrow in Figure 4a for different time scales. As observed in Figure 3d, the quick and slow rises were obtained and are attributable to the mobile (for the E/A/E/A signal) and shallowly trapped (A/E/A/E) CSs, respectively.

Modeling Electron Spin Polarization of the CS States. We presented matrix forms to analyze the TREPR data based

Table 1. Parameters for the Simulations of the Time-Dependent EPR Data (Figure 4) of the Two Photoinduced CS States in the as-spun P3HT:PC$_{61}$BM Blend Film at 77 K

polarization pattern	D (μT)[a]	J (μT)[a]	dipolar angles	T_1 (μs)	T_2 (μs)	T_{23} (μs)	k_T (10^5 s^{-1})[b]	$\lvert V_{CR}\rvert$ (cm^{-1})
E/A/E/A	−100 (±33)	62 (±17)	θ = 65° ϕ = 0°	0.4	< 0.2	0.3		0.6 (±0.1)
A/E/A/E	−530 (±90)	9 (±20)	θ = 45° ϕ = 35°	1.6	3.0	>10	2.5	0.2 (±0.1)

[a]Errors in parentheses were evaluated from the line widths of $1/(2\pi T_{2d}^*)$ and $1/(2\pi T_{2J}^*)$ originating from heterogeneities of $3d$ and $d - 2J$ in the T_0–$T_\pm$ and S–$T_\pm$ transition energies,[17] respectively. (T_{2d}^*, T_{2J}^*) = (65, 75) and (55, 30) ns were employed for the E/A/E/A and A/E/A/E polarizations, respectively, in Figure 4. [b]The triplet CR rate to reproduce the spectrum shapes at t_d = 2.4 μs in the trap CS states.

DOI: 10.1021/acs.jpcc.9b02672
J. Phys. Chem. C 2019, 123, 13472–13481

on the stochastic-Liouville equation (SLE)[17,18,21,39] in the transient CS states with considering the charge-recombination kinetics (k_S and k_T in Figure 1b) and spin relaxations represented by (1) the relaxation time T_{23} between |2> and |3> levels (dashed arrows in Figure 1b) due to the *J*-modulation[53] and (2) the spin−lattice relaxation time T_1 determined by *D* fluctuations.[25,54] We performed the spectrum computations for the two different CS species (Figure S2) having individual EPR parameter sets in Table 1, and summed to fit the MPS spectra (Figure 4) at the three different time-windows by powder-pattern integrations from all possible $\boldsymbol{B}_0$ directions by taking into account their angle distributions in Figure 1a with respect to $\boldsymbol{M}$ for the depolarized, $\boldsymbol{B}_0 \perp \boldsymbol{L}$ and $\boldsymbol{B}_0$ // $\boldsymbol{L}$ conditions,[42,43] as shown by the solid fitting lines in Figure 3 and in Figure 4. More details on the computations are described in the Method section and in Figure S2.

Using *J*, *D*, and angle parameters, we also computed time profiles of the transverse magnetizations, solving a 16 × 16 matrix form[18] for time differential equations in 16 elements (ρ_{++}, ρ_{+S}, ρ_{+0}, ρ_{+-}, ρ_{S+}, ···) of the density matrix from the S, T_+, T_0, and T_- basis functions. In this, we considered the microwave B_1 strength ($\omega_1 = 2.7 \times 10^6$ rad/s) to fit the profiles in Figure 4m,n. $\omega_1 = 6 \times 10^5$ rad/s was utilized for Figure 3d. The spin-relaxation times were estimated for the electron−hole pairs with this analysis (Table 1). The E/A/E/A polarization was deduced to have the mobile charge characteristic from T_1 = 0.4 μs, T_{23} = 0.3 μs, and T_2 < 0.2 μs to reproduce the quick rise and decay of the TREPR signals, as shown by the dotted blue lines in Figure 3d,m. On the other hand, the slow rise and decay in the A/E/A/E component were explained by a larger T_2 being 3.0 μs with T_1 = 1.6 μs and T_{23} = 11 μs (red dotted lines in Figure 4m,n). These slower spin relaxation characteristics than those from the E/A/E/A contribution are evident from the spin nutation effect as the oscillatory feature for t_d > 1 μs in Figure 4n. We confirmed that, when the B_1 field is very weak (microwave power =1.0 mW in Figure S3 vs 6.3 mW in Figure 4m,n), the A/E/A/E component decayed by more than 2 times longer time constants with the disappearance of the oscillatory feature, while the E/A/E/A component increased and decayed quickly, demonstrating the trap and mobile charge characteristics at the BHJ interface, respectively. Table 1 summarizes the EPR and kinetic parameters for the mobile (top) and trap (bottom) electron−hole pairs.

Electron Spin Polarization Imaging of Geometries of Mobile and Trapped CS States. Using the individual TREPR components (Figure S2) employed for the spectrum fittings in Figure 4 obtained by the powder-pattern averaging, one can distribute the ESP intensities of the transverse magnetization to all the field directions at a specified B_0 strength to obtain ESP imaging maps for the mobile and trapped electron−hole pairs (Figure 5a,c, respectively). From Figure 4d−f, the ESP at B_0 = 337.25 mT for the P3HT$^{+\bullet}$ side is highly modulated by the field direction, as shown by the colored dotted arrows. This is because the E/A-resonance field position and its splitting are both changed by the combination of the g_{P3HT} anisotropy and *d*-anisotropy effects; for the g_y direction (Figure 5a), an A signal is obtained at the red dotted arrow in Figure 4e reflecting the largest g_y principal value and the small −4*d*, while an E polarization is resulted (blue dotted arrow in Figure 4f) for the g_x direction due to the higher resonance field by the small g_x and due to the larger −4*d* splitting in the E/A pattern. Furthermore, around the field directions tilted by ca. 30° from the g_y-axis in Figure 5a, it is expected that the absorptive signal intensities become strong because these directions may provide spectrum peak positions at B_0 = 337.25 mT on the A polarization of the E/A pattern (Figure 4e). This means that one may identify the principal g_y-axis from the center direction of the donut-shaped ring (Figure 5a) mapped with the transverse magnetization. Similar donut shapes were observed for the g_x and g_z directions, demonstrating that one may directly identify the orientation of P3HT$^{+\bullet}$ in the CS state from this map. This is relevant to the principal axis assignment in the g_{P3HT} tensor from the MPS effect of the peak position in Figure 4a−c, as described above.

As for the emissive polarization in the E/A/E/A pattern, the E signal in the hole side is expected to be strongest for the field direction parallel to the inter-spin vector because the E/A splitting by −4*d* + 2*J* is largest as described above. Thus, the E signal reaches a peak position at B_0 = 337.25 mT in the field−swept E/A spectrum of Figure 4f. This leads to identifying the **d** vector from the blue mapping region, which corresponds to the direction of the strongest emissive magnetization in Figure 5a. As a result, from this ESPI obtained from the above-mentioned fittings of the MPS data, one may reliably identify the position of the counter PCBM$^{-\bullet}$ from the $\boldsymbol{d}$ vector in the CS state,[25] as schematically drawn in Figure 5b for the mobile E/A/E/A polarization, demonstrating the one-dimensional intrachain hole conduction. Using the same procedure to obtain Figure 5a, we mapped the ESP (Figure 5c) of the A/E/A/E polarization to the several $\boldsymbol{B}_0$ directions to visualize the geometry of the CS state in Figure 5d. In this, the $\boldsymbol{d}$ vector is obtained from the polar direction of the blue emissive map[25] originating from the dipolar interaction because the A/E/A/E spectrum shape is dominated by *D* when *J* is weak (Table 1). This $\boldsymbol{d}$ vector in Figure 5c is tilted at angles of c.a. 50° from the g_x, g_y, and g_z axes equivalently and is coincident with the result (Figure 4g−i) that the EPR spectrum is independent of the $\boldsymbol{L}$ direction. This is consistent with the previous reports that the intermolecular charge separations via the contact CT generates the shallowly trapped state (Figure 5d) at 77 K.[16,21] The separations of the electrons might also take place in the PCBM domain[30] to several directions following the interfacial contact CT because the MPS effect was not observable for the A/E/A/E polarization.

Electronic Couplings and Trap Depths of the CS States. For the mobile electron−hole pairs that exhibited the E/A/E/A polarization, (*J*, *D*) = (62 μT, −100 μT) was essential to interpret the MPS effect, as explained above with Figure 4a−f. From this positive *J*, the electronic coupling (V_{CR}) is estimated to be $|V_{CR}| \approx 0.6$ cm^{-1} using the configuration interaction[56] in $2J$ ($=|V_{CR}|^2/\Delta E_{CR}$) where ΔE_{CR} (≈0.4 eV)[18] is the vertical energy gap for the k_T recombination in Figure 1b, while the spin−spin separation (r_{CC}) is estimated to be r_{CC} = 3.0(±0.4) nm by the point-dipole approximation ($D = -2780/r_{CC}^3$) on the *D* parameter in the unit of μT. This distance is well consistent with a reported center separation in distributed CS distances obtained in the blend films at cryogenic temperatures by Hodgkiss and co-workers.[24] We also obtained (*J*, *D*) = (70 μT, −124 μT) by the spectrum simulation in Figure 3a, leading to $|V_{CR}| \approx 0.6$ cm^{-1} at r_{CC} = 2.9(±0.3) nm in the OSC substrate.

The inter-spin distance and electronic coupling were also estimated for the trap CS state to be r_{CC} = 1.7(±0.1) nm and $|V_{CR}| \approx 0.2$ cm^{-1}, respectively, from (*J*, *D*) = (9 μT, −530 μT) as shown in Table 1. To comprehensibly understand how the electronic interactions are affected by the CS geometries and

DOI: 10.1021/acs.jpcc.9b02672
J. Phys. Chem. C 2019, 123, 13472−13481

by the molecular motions in the present system, the above $|V_{CR}|$ values are plotted vs r_{CC} by filled and open circles for the mobile and trapped charges, respectively, in the blend films including the previous reports[21] obtained by the TREPR analyses at the delay times $t_d > 0.3$ μs, as shown in Figure 6b.

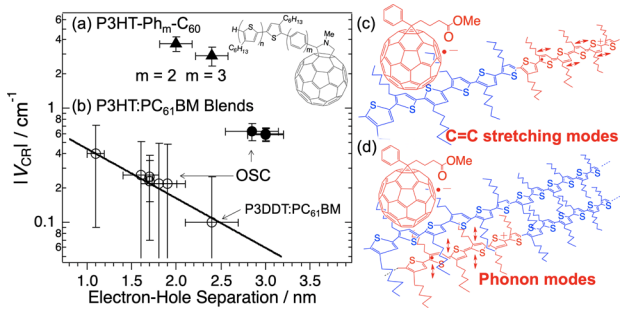

Figure 6. (Left) Semi-log plots of the electronic couplings vs CS distances in poly(3-alkylthiophene-2,5-diyl)-fullerene systems including (a) P3HT−fullerene linked dyads[17] bridged by oligo-p-phenylenes (▲: P3HT-Ph$_m$-C$_{60}$, m = 2, 3). (b) In the blend films, $|V_{CR}|$s of the mobile CSs were obtained from the E/A/E/A patterns at 0.2 μs and are plotted by the filled circles (●). The $|V_{CR}|$s of the trapped CSs were obtained from the SCRP analyses for the later delay times larger than 0.3 μs and are plotted by the open circles (○). Data sources are detailed in Table S1.[18,21] The error bars were derived from the line widths determined by $1/(2\pi T_{2d}^*)$ and $1/(2\pi T_{2J}^*)$ as described in Table 1. (Right) Origins of the heterogeneous charge generations are schematically drawn using arrows as the non-Condon effects by (c) high-frequency modes for the strongly coupled mobile CS states (●) and by (d) low-frequency phonon modes for the weakly coupled trapped CS states (○), respectively.

Several CS geometries including r_{CC} were previously obtained at 77 K by varying the D:A blend ratio and by changing the alkyl side-chain length in poly(3-alkylthiophene), as summarized in Table S1.[18,21] These interfacial CSs were treated as the weakly trapped charges in the blend films.[16] For comparison, reported $|V_{CR}|$ values are also plotted (filled triangles in Figure 6a) on the primary photoinduced CS states in poly(3-hexylthiophene)−fullerene linked dyads bridged by rigid oligo-p-phenylene spacers (P3HT-Ph$_m$-C$_{60}$, m = 2, 3 in Figure 6a)[17] as the long-range coupling via through-bond interactions. The larger electronic interactions of $|V_{CR}| \approx 0.6$ cm^{-1} (● in Figure 6b) for the separated charges ($r_{CC} \approx 3$ nm) than those (○ in Figure 6b) in the trapped charges in Figure 5d are explained by the intrachain interaction through the polymer backbone nearby the hole; the bridge mediated tunneling via the backbone which is directly π-stack on the PCBM$^{-\bullet}$ moiety (as shown by the dotted line in Figure 5b) may induce the stronger electronic tunneling between the unpaired orbitals. Alternately, highly delocalized intrachain hole distribution in the backbone[30] would facilitate the strong electronic interaction between the charges while the spin−spin dipolar interaction becomes weak, because the one-dimensional hole delocalization after the photoinduced CS was observed in the P3HT-Ph$_m$-C$_{60}$ linked systems.[17] In this respect, the highly strong electronic interactions $|V_{CR}| \approx 3$ cm^{-1} (▲ in Figure 6a) were explained by the strong through-bond coupling via the oligophenylene bridges, as reported previously.[17] The shorter spin-relaxation times in the mobile charges in Table 1 are thus very likely to be resulted from the one-dimensional intrachain charge-motion and are coincident with the reported CWEPR studies on the origins of small T_1 and T_2 of the polymer polarons in P3HT:PCBM composites at lower temperatures.[19,20]

As for the trapped CS states ($|V_{CR}| \approx 0.2$ cm^{-1} at $r_{CC} \approx 1.7$ nm as plotted by ○ in Figure 6), the weakened electronic interaction is explained by intermolecular couplings, as represented by Figure 5d; although the intervening polymer chains participate in mediating the tunneling interactions in V_{CR},[16] the involvement of the polymer−polymer through-space interactions (V_{BB}) should result in the weaker $|V_{CR}|$ than in the case of Figure 5b. From the superexchange model, the distance dependence of $|V_{CR}|$ has been characterized by the attenuation factor (β) in $|V_{CR}| = V_d \exp[-\beta (r_{CC} - d)/2]$ where d denotes contact D:A separation. According to the McConnell's electron-tunneling mechanism, the attenuation degree has been approximated as follows,[16,21,57]

$$\beta = \frac{2}{d_{BB}} \ln\left(\frac{\Delta E_{eff}}{V_{BB}}\right) \quad (1)$$

where ΔE_{eff} and V_{BB} represent the trap depth (i.e., the tunneling barrier) and the bridge−bridge coupling at the d_{BB} separation, respectively. The trap characteristics derived from the larger T_1 and T_2 in Table 1 may originate from the electrostatic attraction between the charges in Figure 5d;[16] the electron−hole pairs in Figure 5d are thus frozen at 77 K at $r_{CC} \approx 1.7$ nm. Such a binding potential is weaker for the 3 nm separated (or 1D delocalized) charges in Figure 5b than in the trapped CS, allowing the 1D hole motions in the polymer chains. This is well consistent with the shorter T_1 and T_2 values in the E/A/E/A polarization in Table 1. The line fit in Figure 6b to the group of the open circles denotes that the trapped CS states for $t_d > 0.3$ μs were explained by the above attenuation with $\beta = 2$ nm^{-1}.[21] From this, $\Delta E_{eff} \approx 0.2$ eV, which was comparable to V_{BB} was estimated as the tunneling barrier from the unpaired orbital level in P3HT$^{+\bullet}$ to the highest occupied molecular orbitals (HOMO) of the single P3HT chains.[16,21] This indicated that the trap depths by the Coulomb bindings are shallow enough to be detrapped[17,58] to contribute to the photocurrent at room temperature. This "shallowness" is also relevant to preferential triplet CR[59] deactivation in Table 1 with $|V_{CR}| \approx 0.2$ cm^{-1} from the trapped CS states,[18] because the CS state energy level is required to be as high as the triplet energy (1.65 eV) of ^{3}P3HT*,[60] which is close to the P3HT-PC$_{61}$BM HOMO−lowest unoccupied molecular orbital band offset,[52] denoting very weak electrostatic stabilization in the trapped CS.

In Figure 6b, the filled circles are deviated from the line on the trapped CSs and exhibit strong electronic interactions for the highly separated charge pairs, representing long-range hole-conducting characteristics through a single polymer chain[61] as described above. This is interpreted by a very small effective value in $\Delta E_{eff}/V_{BB}$ of eq 1 due to the strong intrachain coupling. The Coulomb binding with $\Delta E_{eff} < 0.2$ eV is thus conclusive for the mobile CS state and is consistent with the geometry in Figure 5b to be detrapped as was demonstrated in the P3HT-Ph$_m$-C$_{60}$ systems at room temperature.[17]

Origin of the Heterogenous CS Geometries and Mobilities. In our previous reports, it was suggested that the e−p coupling may play a role for the distant CS; the coupling of the hole to the librations of the P3AT crystalline domains would facilitate the separated charge generations.[16,21] For understanding the present coexistence of the mobile and trapped CS states with different geometries, we propose that

DOI: 10.1021/acs.jpcc.9b02672
J. Phys. Chem. C 2019, 123, 13472−13481

several molecular motions participate in creating the different CS states, as schematically drawn at the right panel in Figure 6 in terms of the non-Condon effect.[8,23,62] When a high-frequency C=C stretching vibration is coupled to regenerate the quinoid structure[62,63] in P3HT$^{+\bullet}$ upon the hole conduction (Figure 6c), it is anticipated that the hole separation occurs within the aromatic backbone. On the other hand, when the polymer−polymer interchain motions are rather coupled, the interpolymer hole separations are also plausible to result in the CS state in Figure 6d. This interpretation is well consistent with the theoretical prediction by Vukmirović et al.[64] that the charge conductions were promoted by the e−p couplings in which several phonon modes were participating to result in the scattering behavior in the electronic attenuation (β) for the hole transfers, as is herein observed by the ● plots deviated from the straight line in Figure 6b. The involvement of the C=C stretching vibration for the hole generation was demonstrated by a recent ultrafast two-dimensional electronic spectroscopic observation of the vibration quantum coherence with a frequency of 1506 cm^{-1} in P3HT/PCBM aggregates, as reported by Song et al.[65] and correlates with the mobile charge pair geometry as shown in Figure 5b. Concerning the trap CS state (Figures 5d and 6d), the intermolecular libration modes and the disorder alkyl side-chain motions may also play roles for the interchain dissociations.[21] Although such low-frequency phonons seem not to be significant for the photocurrent at the present temperatures resulting in the frozen trap at 1.7 nm, these modes are crucial for the OSC operations at room temperature to cause detrapping[16] (vide supra). This is because such low-frequency modes numerously exist in the solid aggregates including the $PC_{61}BM$ clusters and may enhance the density of the states for the separated electron−hole pairs coupled with the dense phonon bath,[16] in contrast to the C=C high-frequency mode in the single polymer chain. Analysis of temperature dependence on the TREPR data would be informative to track detrapping in the blend films, as 1D charge-hopping dissociations were characterized in the P3HT-Ph$_m$-C_{60} systems at room temperature.[17]

CONCLUSIONS

In conclusion, we have deduced the motional characters, the geometries, and the electronic couplings of the two different photoinduced electron−hole pairs simultaneously generated in the P3HT-crystal/PCBM interfaces of the blend films including the OSC substrate using TREPR analysis with the applications of the ESPI method at cryogenic temperature. The former E/A/E/A polarizations exhibited the MPS effect and originated from the mobile conducting charge pairs in which the holes would be delocalized one-dimensionally in the P3HT aromatic plane to which $PC_{61}BM^{-\bullet}$ is stuck. The latter A/E/A/E polarizations, on the other hand, possess the trap charge pair characteristics weakly bound by the electrostatic interactions at 77 K. The coexistence of intrachain and intermolecular photoinduced interfacial charge-motions are proposed to be resulted from the multiple phonon modes as the non-Condon effect in the aggregated organic materials.[62] In Figure 5b, vibrationally hot states could be involved in the 1D-mobile charges.[8,23] That is, high-frequency in-plane vibrations or reorganizations[66] within the aromatic backbone leading to the quinoid formation in P3HT$^{+\bullet}$ would be associated with the photoinduced 1D charge separation as shown in Figure 6c, while the intermolecular libration modes and the disorder alkyl side-chain motions may play roles for the intermolecular dissociations as shown in Figure 6d.[21] The low-frequency phonons may be crucial for the OSC operations at room temperature because such low-frequency modes in Figure 5d and also in the $PC_{61}BM$ clusters may enhance the density of the states for the separated electron−hole pairs coupled with the dense phonon bath.[16] The present study thus implies that the three-dimensional imaging analysis of the spin polarization is powerful to understand the heterogeneous phonon-assisted photoinduced processes by mapping the transverse magnetizations by the transient spins based on SLE analysis that fully explains the MPS spectra and their time profiles in the anisotropic systems.

ASSOCIATED CONTENT

Supporting Information

The Supporting Information is available free of charge on the ACS Publications website at DOI: 10.1021/acs.jpcc.9b02672.

Sample conditions; decompositions of the computed transient EPR signals; time profile of the TREPR signal obtained at the microwave power of 1.0 mW; parameters for the simulations of the time-dependent EPR data; and MPS data for another blend film (PDF)

AUTHOR INFORMATION

Corresponding Author

*E-mail: ykobori@kitty.kobe-u.ac.jp.

ORCID

Yasuhiro Kobori: 0000-0001-8370-9362
Takashi Tachikawa: 0000-0001-6465-5792
Kazuhiro Marumoto: 0000-0001-9792-0775

Notes

The authors declare no competing financial interest.

ACKNOWLEDGMENTS

This work is dedicated to the deceased former Prof. Kimio Akiyama (Tohoku University). This work was supported by a Grant-in-Aid for Scientific Research (Nos. JP17K19105, JP16H04097, and JP19H00888) from the Ministry of Education, Culture, Sports, Science and Technology (MEXT), Japan.

REFERENCES

(1) Zhang, S.; Qin, Y.; Zhu, J.; Hou, J. Over 14% Efficiency in Polymer Solar Cells Enabled by a Chlorinated Polymer Donor. *Adv. Mater.* **2018**, *30*, No. 1800868.

(2) Li, S.; Ye, L.; Zhao, W.; Yan, H.; Yang, B.; Liu, D.; Li, W.; Ade, H.; Hou, J. A Wide Band Gap Polymer with a Deep Highest Occupied Molecular Orbital Level Enables 14.2% Efficiency in Polymer Solar Cells. *J. Am. Chem. Soc.* **2018**, *140*, 7159−7167.

(3) Kim, H.-S.; Hagfeldt, A.; Park, N.-G. Morphological and Compositional Progress in Halide Perovskite Solar Cells. *Chem. Commun.* **2019**, *55*, 1192−1200.

(4) Huang, Y.; Kramer, E. J.; Heeger, A. J.; Bazan, G. C. Bulk Heterojunction Solar Cells: Morphology and Performance Relationships. *Chem. Rev.* **2014**, *114*, 7006−7043.

(5) Kawashima, K.; Fukuhara, T.; Suda, Y.; Suzuki, Y.; Koganezawa, T.; Yoshida, H.; Ohkita, H.; Osaka, I.; Takimiya, K. Implication of Fluorine Atom on Electronic Properties, Ordering Structures, and Photovoltaic Performance in Naphthobisthiadiazole Based Semiconducting Polymers. *J. Am. Chem. Soc.* **2016**, *138*, 10265−10275.

(6) Zhao, W. C.; Li, S. S.; Yao, H. F.; Zhang, S. Q.; Zhang, Y.; Yang, B.; Hou, J. H. Molecular Optimization Enables over 13% Efficiency in Organic Solar Cells. *J. Am. Chem. Soc.* **2017**, *139*, 7148−7151.

DOI: 10.1021/acs.jpcc.9b02672
J. Phys. Chem. C 2019, 123, 13472−13481

(7) Wang, C.; Nakano, K.; Lee, H. F.; Chen, Y. J.; Hong, Y. L.; Nishiyama, Y.; Tajima, K. Intermolecular Arrangement of Fullerene Acceptors Proximal to Semiconducting Polymers in Mixed Bulk Heterojunctions. *Angew. Chem., Int. Ed.* **2018**, *57*, 7034−7039.
(8) Shimazaki, T.; Nakajima, T. Theoretical Study on the Cooperative Exciton Dissociation Process Based on Dimensional and Hot Charge-Transfer State Effects in an Organic Photocell. *J. Chem. Phys.* **2016**, *144*, No. 234906.
(9) Grancini, G.; Maiuri, M.; Fazzi, D.; Petrozza, A.; Egelhaaf, H. J.; Brida, D.; Cerullo, G.; Lanzani, G. Hot Exciton Dissociation in Polymer Solar Cells. *Nat. Mater.* **2013**, *12*, 29−33.
(10) Vandewal, K.; Albrecht, S.; Hoke, E. T.; Graham, K. R.; Widmer, J.; Douglas, J. D.; Schubert, M.; Mateker, W. R.; Bloking, J. T.; Burkhard, G. F.; et al. Efficient Charge Generation by Relaxed Charge-Transfer States at Organic Interfaces. *Nat. Mater.* **2014**, *13*, 63−68.
(11) Hood, S. N.; Kassal, I. Entropy and Disorder Enable Charge Separation in Organic Solar Cells. *J. Phys. Chem. Lett.* **2016**, *7*, 4495−4500.
(12) Janković, V.; Vukmirovic, N. Combination of Charge Delocalization and Disorder Enables Efficient Charge Separation at Photoexcited Organic Bilayers. *J. Phys. Chem. C* **2018**, *122*, 10343−10359.
(13) Pace, N. A.; Reid, O. G.; Rumbles, G. Delocalization Drives Free Charge Generation in Conjugated Polymer Films. *ACS Energy Lett.* **2018**, *3*, 735−741.
(14) Clarke, T. M.; Durrant, J. R. Charge Photogeneration in Organic Solar Cells. *Chem. Rev.* **2010**, *110*, 6736−6767.
(15) Guo, J. M.; Ohkita, H.; Benten, H.; Ito, S. Charge Generation and Recombination Dynamics in Poly(3-hexylthiophene)/Fullerene Blend Films with Different Regioregularities and Morphologies. *J. Am. Chem. Soc.* **2010**, *132*, 6154−6164.
(16) Kobori, Y.; Miura, T. Overcoming Coulombic Traps: Geometry and Electronic Characterizations of Light-Induced Separated Spins at the Bulk Heterojunction Interface. *J. Phys. Chem. Lett.* **2015**, *6*, 113−123.
(17) Miura, T.; Tao, R.; Shibata, S.; Umeyama, T.; Tachikawa, T.; Imahori, H.; Kobori, Y. Geometries, Electronic Couplings, and Hole Dissociation Dynamics of Photoinduced Electron−Hole Pairs in Polyhexylthiophene−Fullerene Dyads Rigidly Linked by Oligophenylenes. *J. Am. Chem. Soc.* **2016**, *138*, 5879−5885.
(18) Kobori, Y.; Noji, R.; Tsuganezawa, S. Initial Molecular Photocurrent: Nanostructure and Motion of Weakly Bound Charge-Separated State in Organic Photovoltaic Interface. *J. Phys. Chem. C* **2013**, *117*, 1589−1599.
(19) Krinichnyi, V. I.; Yudanova, E. I.; Spitsina, N. G. Light-Induced Electron Paramagnetic Resonance Study of Poly(3-alkylthiophene)/Fullerene Composites. *J. Phys. Chem. C* **2010**, *114*, 16756−16766.
(20) Krinichnyi, V. I.; Yudanova, E. I. Light-Induced EPR Study of Charge Transfer in P3HT/PC71BM Bulk Heterojunctions. *J. Phys. Chem. C* **2012**, *116*, 9189−9195.
(21) Miura, T.; Aikawa, M.; Kobori, Y. Time-Resolved EPR Study of Electron-Hole Dissociations Influenced by Alkyl Side Chains at the Photovoltaic Polyalkylthiophene:PCBM Interface. *J. Phys. Chem. Lett.* **2014**, *5*, 30−35.
(22) Bakulin, A. A.; Rao, A.; Pavelyev, V. G.; van Loosdrecht, P. H. M.; Pshenichnikov, M. S.; Niedzialek, D.; Cornil, J.; Beljonne, D.; Friend, R. H. The Role of Driving Energy and Delocalized States for Charge Separation in Organic Semiconductors. *Science* **2012**, *335*, 1340−1344.
(23) Tamura, H.; Burghardt, I. Ultrafast Charge Separation in Organic Photovoltaics Enhanced by Charge Delocalization and Vibronically Hot Exciton Dissociation. *J. Am. Chem. Soc.* **2013**, *135*, 16364−16367.
(24) Barker, A. J.; Chen, K.; Hodgkiss, J. M. Distance Distributions of Photogenerated Charge Pairs in Organic Photovoltaic Cells. *J. Am. Chem. Soc.* **2014**, *136*, 12018−12026.
(25) Hasegawa, M.; Nagashima, H.; Minobe, R.; Tachikawa, T.; Mino, H.; Kobori, Y. Regulated Electron Tunneling of Photoinduced Primary Charge-Separated State in the Photosystem II Reaction Center. *J. Phys. Chem. Lett.* **2017**, *8*, 1179−1184.
(26) Closs, G. L.; Forbes, M. D. E.; Norris, J. R. Spin-Polarized Electron-Paramagnetic Resonance-Spectra of Radical Pairs in Micelles - Observation of Electron-Spin Spin Interactions. *J. Phys. Chem.* **1987**, *91*, 3592−3599.
(27) Hore, P. J.; Hunter, D. A.; McKie, C. D.; Hoff, A. J. Electron Paramagnetic Resonance of Spin-Correlated Radical Pairs in Photosynthetic Reactions. *Chem. Phys. Lett.* **1987**, *137*, 495−500.
(28) Avdievich, N. I.; Forbes, M. D. E. Dynamic Effects in Spin-Correlated Radical Pair Theory: J Modulation and a New Look at the Phenomenon of Alternating Line Widths in the EPR Spectra of Flexible Biradicals. *J. Phys. Chem.* **1995**, *99*, 9660−9667.
(29) Weber, S.; Biskup, T.; Okafuji, A.; Marino, A. R.; Berthold, T.; Link, G.; Hitomi, K.; Getzoff, E. D.; Schleicher, E.; Norris, J. R. Origin of Light-Induced Spin-Correlated Radical Pairs in Cryptochrome. *J. Phys. Chem. B* **2010**, *114*, 14745−14754.
(30) Niklas, J.; Poluektov, O. G. Charge Transfer Processes in OPV Materials as Revealed by EPR Spectroscopy. *Adv. Energy Mater.* **2017**, *7*, No. 1602226.
(31) Uvarov, M. N.; Kulik, L. Electron Spin Echo of Photoinduced Spin-Correlated Polaron Pairs in P3HT:PCBM Composite. *Appl. Magn. Reson.* **2013**, 97−106.
(32) Behrends, J.; Sperlich, A.; Schnegg, A.; Biskup, T.; Teutloff, C.; Lips, K.; Dyakonov, V.; Bittl, R. Direct Detection of Photoinduced Charge Transfer Complexes in Polymer Fullerene Blends. *Phys. Rev. B* **2012**, *85*, No. 125206.
(33) Kraffert, F.; Behrends, J. Spin-Correlated Doublet Pairs as Intermediate States in Charge Separation Processes. *Mol. Phys.* **2017**, *115*, 2373−2386.
(34) Kraffert, F.; Steyrleuthner, R.; Albrecht, S.; Neher, D.; Scharber, M. C.; Bittl, R.; Behrends, J. Charge Separation in PCPDTBT:PCBM Blends from an EPR Perspective. *J. Phys. Chem. C* **2014**, *118*, 28482−28493.
(35) Aguirre, A.; Gast, P.; Orlinskii, S.; Akimoto, I.; Groenen, E. J. J.; El Mkami, H.; Goovaerts, E.; Van Doorslaer, S. Multifrequency EPR analysis of the positive polaron in I-2-doped poly(3-hexylthiophene) and in poly[2-methoxy-5-(3,7-dimethyloctyloxy)]-1,4-phenylenevinylene. *Phys. Chem. Chem. Phys.* **2008**, *10*, 7129−7138.
(36) De Ceuster, J.; Goovaerts, E.; Bouwen, A.; Hummelen, J. C.; Dyakonov, V. High-Frequency (95 GHz) Electron Paramagnetic Resonance Study of the Photoinduced Charge Transfer in Conjugated Polymer-Fullerene Composites. *Phys. Rev. B* **2001**, *64*, No. 195206.
(37) Watanabe, S.-i.; Tanaka, H.; Kuroda, S.-i.; Toda, A.; Nagano, S.; Seki, T.; Kimoto, A.; Abe, J. Electron Spin Resonance Observation of Field-Induced Charge Carriers in Ultrathin-Film Transistors of Regioregular Poly(3-hexylthiophene) with Controlled In-Plane Chain Orientation. *Appl. Phys. Lett.* **2010**, *96*, No. 173302.
(38) Kouki, F.; Spearman, P.; Valat, P.; Horowitz, G.; Garnier, F. Experimental Determination of Excitonic Levels in Alpha-Oligothiophenes. *J. Chem. Phys.* **2000**, *113*, 385−391.
(39) Kobori, Y.; Ponomarenko, N.; Norris, J. R. Time-Resolved Electron Paramagnetic Resonance Study on Cofactor Geometries and Electronic Couplings after Primary Charge Separations in the Photosynthetic Reaction Center. *J. Phys. Chem. C* **2015**, *119*, 8078−8088.
(40) Till, U.; Klenina, I. B.; Proskuryakov, I. I.; Hoff, A. J.; Hore, P. J. Recombination Dynamics and EPR Spectra of the Primary Radical Pair in Bacterila Photosynthetic Reaction Centers with Blocked Electron Transfer to the Primary Acceptor. *J. Phys. Chem. B* **1997**, *101*, 10939−10948.
(41) Nagamori, T.; Marumoto, K. Direct Observation of Hole Accumulation in Polymer Solar Cells During Device Operation using Light-Induced Electron Spin Resonance. *Adv. Mater.* **2013**, *25*, 2362−2367.
(42) Kobori, Y.; Fuki, M. Protein−Ligand Structure and Electronic Coupling of Photoinduced Charge-Separated State: 9,10-Anthraquinone-1-sulfonate Bound to Human Serum Albumin. *J. Am. Chem. Soc.* **2011**, *133*, 16770−16773.

DOI: 10.1021/acs.jpcc.9b02672
J. Phys. Chem. C 2019, 123, 13472−13481

(43) Fuki, M.; Murai, H.; Tachikawa, T.; Kobori, Y. Time Resolved EPR Study on the Photoinduced Long-Range Charge-Separated State in Protein: Electron Tunneling Mediated by Arginine Residue in Human Serum Albumin. *J. Phys. Chem. B* **2016**, *120*, 4365−4372.
(44) Ema, F.; Tanabe, M.; Saito, S.; Yoneda, T.; Sugisaki, K.; Tachikawa, T.; Akimoto, S.; Yamauchi, S.; Sato, K.; Osuka, A.; et al. Charge-Transfer Character Drives Möbius Antiaromaticity in the Excited Triplet State of Twisted [28]Hexaphyrin. *J. Phys. Chem. Lett.* **2018**, *9*, 2685−2690.
(45) Borovykh, I. V.; Proskuryakov, I. I.; Klenina, I. B.; Gast, P.; Hoff, A. J. Magnetophotoselection Study of the Lowest Excited Triplet State of the Primary Donor in Photosynthetic Bacteria. *J. Phys. Chem. B* **2000**, *104*, 4222−4228.
(46) Regev, A.; Michaeli, S.; Levanon, H.; Cyr, M.; Sessler, J. L. Solvent Effect in Randomly and Partially Oriented Triplets of the Sapphyrin Dication: Optical and Fast EPR-Magnetophotoselection Measurements. *J. Phys. Chem.* **1991**, *95*, 9121−9129.
(47) Kobori, Y.; Yamauchi, S.; Akiyama, K.; Tero-Kubota, S.; Imahori, H.; Fukuzumi, S.; Norris, J. R. Primary Charge-Recombination in an Artificial Photosynthetic Reaction Center. *Proc. Natl. Acad. Sci. U.S.A.* **2005**, *102*, 10017−10022.
(48) Norris, J. R.; Morris, A. L.; Thurnauer, M. C.; Tang, J. A General-Model of Electron-Spin Polarization Arizing From the Interactions within Radical Pairs. *J. Chem. Phys.* **1990**, *92*, 4239−4249.
(49) Morris, A. L.; Snyder, S. W.; Zhang, Y. N.; Tang, J.; Thurnauer, M. C.; Dutton, P. L.; Robertson, D. E.; Gunner, M. R. Electron-Spin Polarization Model Applied to Sequential Electron-Transfer in Iron-Containing Photosynthetic Bacterial Reaction Centers with Different Quinones as Q(a). *J. Phys. Chem.* **1995**, *99*, 3854−3866.
(50) Huang, Y.-C.; Tsao, C.-S.; Chuang, C.-M.; Lee, C.-H.; Hsu, F.-H.; Cha, H.-C.; Chen, C.-Y.; Lin, T.-H.; Su, C.-J.; Jeng, U. S.; et al. Small- and Wide-Angle X-ray Scattering Characterization of Bulk Heterojunction Polymer Solar Cells with Different Fullerene Derivatives. *J. Phys. Chem. C* **2012**, *116*, 10238−10244.
(51) Tamai, Y.; Matsuura, Y.; Ohkita, H.; Benten, H.; Ito, S. One-Dimensional Singlet Exciton Diffusion in Poly(3-hexylthiophene) Crystalline Domains. *J. Phys. Chem. Lett.* **2014**, *5*, 399−403.
(52) Lee, J.; Vandewal, K.; Yost, S. R.; Bahlke, M. E.; Goris, L.; Baldo, M. A.; Manca, J. V.; Van Voorhis, T. Charge Transfer State Versus Hot Exciton Dissociation in Polymer-Fullerene Blended Solar Cells. *J. Am. Chem. Soc.* **2010**, *132*, 11878−11880.
(53) Fukuju, T.; Yashiro, H.; Maeda, K.; Murai, H.; Azumi, T. Singlet-Born SCRP Observed in the Photolysis of Tetraphenylhydrazine in an SDS Micelle: Time Dependence of the Population of the Spin States. *J. Phys. Chem. A* **1997**, *101*, 7783−7786.
(54) Miura, T.; Murai, H. Effect of Molecular Diffusion on the Spin Dynamics of a Micellized Radical Pair in Low Magnetic Fields Studied by Monte Carlo Simulation. *J. Phys. Chem. A* **2015**, *119*, 5534−5544.
(55) Kayunkid, N.; Uttiya, S.; Brinkmann, M. Structural Model of Regioregular Poly(3-hexylthiophene) Obtained by Electron Diffraction Analysis. *Macromolecules* **2010**, *43*, 4961−4967.
(56) Kobori, Y.; Sekiguchi, S.; Akiyama, K.; Tero-Kubota, S. Chemically Induced Dynamic Electron Polarization Study on the Mechanism of Exchange Interaction in Radical Ion Pairs Generated by Photoinduced Electron Transfer Reactions. *J. Phys. Chem. A* **1999**, *103*, 5416−5424.
(57) Mcconnell, H. Intramolecular Charge Transfer in Aromatic Free Radicals. *J. Chem. Phys.* **1961**, *35*, 508−515.
(58) Goldsmith, R. H.; Sinks, L. E.; Kelley, R. F.; Betzen, L. J.; Liu, W. H.; Weiss, E. A.; Ratner, M. A.; Wasielewski, M. R. Wire-Like Charge Transport at Near Constant Bridge Energy through Fluorene Oligomers. *Proc. Natl. Acad. Sci. U.S.A.* **2005**, *102*, 3540−3545.
(59) Shoji, R.; Omori, T.; Wakikawa, Y.; Miura, T.; Ikoma, T. Magnetoconductance Study on Nongeminate Recombination in Solar Cell Using Poly(3-hexylthiophene) and [6,6]-Phenyl-C-61-butyric Acid Methyl Ester. *ACS Omega* **2018**, *3*, 9369−9377.
(60) Monkman, A. P.; Burrows, H. D.; Hartwell, L. J.; Horsburgh, L. E.; Hamblett, I.; Navaratnam, S. Triplet Energies of pi-Conjugated Polymers. *Phys. Rev. Lett.* **2001**, *86*, 1358−1361.
(61) Li, B.; Yu, H.; Montoto, E. C.; Liu, Y.; Li, S.; Schwieter, K.; Rodríguez-López, J.; Moore, J. S.; Schroeder, C. M. Intrachain Charge Transport through Conjugated Donor−Acceptor Oligomers. *ACS Appl. Electron. Mater.* **2019**, *1*, 7−12.
(62) Kilina, S.; Kilin, D.; Tretiak, S. Light-Driven and Phonon-Assisted Dynamics in Organic and Semiconductor Nanostructures. *Chem. Rev.* **2015**, *115*, 5929−5978.
(63) Luo, J.; Piette, B. M. A. G. Directed Polaron Propagation in Linear Polypeptides Induced by Intramolecular Vibrations and External Electric Pulses. *Phys. Rev. E* **2018**, *98*, No. 012401.
(64) Vukmirović, N.; Wang, L. W. Carrier Hopping in Disordered Semiconducting Polymers: How Accurate is the Miller−Abrahams Model? *Appl. Phys. Lett.* **2010**, *97*, No. 043305.
(65) Song, Y.; Clafton, S. N.; Pensack, R. D.; Kee, T. W.; Scholes, G. D. Vibrational Coherence Probes the Mechanism of Ultrafast Electron Transfer in Polymer-Fullerene Blends. *Nat. Commun.* **2014**, *5*, No. 4933.
(66) Nagasawa, Y.; Yartsev, A. P.; Tominaga, K.; Bisht, P. B.; Johnson, A. E.; Yoshihara, K. Dynamical Aspects of Ultrafast Intermolecular Electron-Transfer Faster Than Solvation Process - Substituent Effects and Energy-Gap Dependence. *J. Phys. Chem.* **1995**, *99*, 653−662.

DOI: 10.1021/acs.jpcc.9b02672
J. Phys. Chem. C 2019, 123, 13472−13481